

This is the accepted manuscript made available via CHORUS. The article has been published as:

Epitaxial $\text{Pb}(\text{Zr,Ti})\text{O}_3$ Ultrathin Films under Open-Circuit Electrical Boundary Conditions

David Sichuga and L. Bellaiche

Phys. Rev. Lett. **106**, 196102 — Published 12 May 2011

DOI: [10.1103/PhysRevLett.106.196102](https://doi.org/10.1103/PhysRevLett.106.196102)

Epitaxial Pb(Zr,Ti)O₃ Ultrathin Films under Open-Circuit Electrical Boundary Conditions

David Sichuga¹ and L. Bellaiche²

¹*Physics Department, Augusta Technical College, Augusta, Georgia, 30906, USA*

²*Physics Department, University of Arkansas, Fayetteville, Arkansas, 72701, USA*

The temperature-versus-misfit-strain phase diagram of Pb(Zr,Ti)O₃ ultrathin films under open-circuit electrical boundary conditions is simulated via the use of an effective Hamiltonian. Two novel phases, both exhibiting *dipolar nanodomains and oxygen octahedral tilting*, are discovered. The interplay between dipolar, antiferrodistortive, alloying and strain degrees of freedom induces several striking features in these two phases, such as the chemical pinning of domain walls, the enhancement of oxygen octahedral tilting near the domain walls, the existence of dipolar waves and cylindrical dipolar chiral “bubbles”.

PACS numbers: 68.55.-a, 77.84.Cg, 77.80.bn, 77.22.Ej, 77.80.B-

The potential of ferroelectric (FE) thin films for miniaturized devices has generated a vast amount of studies devoted to these low-dimensional materials (see, e.g., Refs. [1-3] and references therein). It is now well established that two different boundary conditions, namely electrical and mechanical, play a crucial role on the properties of these systems. For instance, *FE* thin films under short-circuit-like electrical conditions (for which the depolarizing field vanishes or is rather small, as a result of a large screening of the polarization-induced surface charges) exhibit different directions for the spontaneous polarization and different resulting crystallographic phases, depending on the misfit strain arising from the substrate on top of which the film is grown [4-7]. Furthermore, *FE* ultrathin films subject to a relatively large compressive strain but being under open-circuit-like boundary conditions (for which no screening of the polarization-induced surface charges is possible) have been reported to exhibit striking dipolar *nanostripe* domains [8,9] – in order to remove the depolarizing field. Surprisingly, the temperature-versus-misfit-strain phase diagram of these 2D materials is only known for short-circuit-like boundary conditions [4-10]. It is thus, e.g., presently unclear how the recently discovered laminar nanodomains evolve with strain in these compounds, despite the possibility of generating novel structural phases. Moreover, several ferroelectrics -- including the important $\text{Pb}(\text{Zr}_{1-x}\text{Ti}_x)\text{O}_3$ (PZT) solid solutions [11-13] -- can exhibit another degree of freedom in addition to electric dipoles, that is, the oxygen octahedral tilting, which is also termed the *antiferrodistortive* (AFD) motion [14-19]. Another currently unknown issue is how these *AFD* motions affect, or react to, dipolar nanostripes. For instance, it is legitimate to wonder if the interactions between these *AFD* motions and dipolar nanostripes give rise to novel phenomena, based, e.g., on the fact that the coupling between tilting of oxygen octahedra and dipolar vortices yields original chiral *AFD* patterns in zero-dimensional ferroelectrics [20].

The broad aim of this Letter is to address all the aforementioned open questions in PZT ultrathin films being under *open-circuit* (OC) *electrical boundary conditions* and subject to a wide range of strain, via the use of a first-principles-based numerical scheme. The complete temperature-versus-misfit-strain phase diagram of such system is computed for the first time, to the best of our knowledge. Two original phases and various novel phenomena -- that originate from the interplay between *strain*, *alloying*, *dipolar* and *AFD* degrees of freedom -- are discovered. Examples of such phenomena are the pinning of the domain walls around Zr-rich regions, the enhancement of oxygen octahedral tilting near the domain walls, dipolar waves and chiral cylindrical bubbles moving towards the surface as the strain is varied.

We model an epitaxial (001) film made of disordered $\text{Pb}(\text{Zr}_{1-x}\text{Ti}_x)\text{O}_3$ solid solutions. The Ti composition is 48%, which corresponds to the center of the morphotropic phase boundary in the bulk [11,12,14]. Such film is mimicked by a $12 \times 12 \times 12$ supercell that is periodic along the x and y axes (that lie along the pseudo-cubic [100] and [010] directions, respectively) and that is *finite* along the *non-periodic* z axis (that is along the [001] pseudo-cubic direction) – in order to take into account that a real film possesses a surface that can influence its properties. This film therefore has a thickness of 4.8 nm. Its total internal energy, E_{tot} , is provided by the first-principles-derived effective Hamiltonian of Ref. [10], at the sole exception that the film is under open-circuit, rather than close-circuit, electrical boundary conditions [21]. The degrees of freedom are: the \mathbf{u}_i local soft mode in all unit cells i (which is proportional to the electric dipole in the cell i and that is centered on the Ti or Zr -site of that cell i [22]); inhomogeneous strain variables [22]; the η_H homogeneous strain tensor [22]; and the $\boldsymbol{\omega}_i$ pseudo-vectors (that are also centered on the Ti or Zr -sites i) characterizing the direction and magnitude of *AFD* motions in the unit cell i . For instance, $\boldsymbol{\omega}_i = 0.1\mathbf{z}$ corresponds to a rotation of the oxygen octahedra of cell i by 0.1 radians about the z -axis – when denoting \mathbf{z} as the unit vector along the z -axis. The couplings between *FE*, *AFD*, *alloying* and *strain* variables are included [10]. The misfit strain between the film and the substrate [5-7] is defined as $\delta = (a_{\text{sub}}/a_{\text{ref}}) - 1$, where a_{sub} is the in-plane lattice constant of the substrate and where $a_{\text{ref}} = 4.04 \text{ \AA}$ is the lattice constant of the PZT bulk at its cubic-to-tetragonal transition. $\delta > 0$ or $\delta < 0$ characterizes a tensile or compressive misfit strain, respectively. Such misfit strains are mimicked in our simulations by imposing that $\eta_{H,1} = \eta_{H,2} = \delta$. Another component of the homogeneous strain tensor is also frozen, namely (in Voigt notation) $\eta_{H,6} = 0$, to fully model mechanical boundary conditions that are consistent with an epitaxial growth of (001) films. More details of the numerical method presently used can be found in Ref. [10]. Note that effective Hamiltonian approaches have been shown to accurately reproduce the dipolar nanostripe domains of ferroelectric ultrathin films being under compressive strain and *OC* boundary conditions [8,9], in addition to describe the complex phase diagram of PZT bulks [14]. Here, the total energy of the effective Hamiltonian is used in Monte Carlo (MC) simulations, with up to 3×10^5 MC sweeps and by progressively cooling the system, to compute properties of the studied epitaxial PZT film, at any finite temperature.

Figure 1 shows the predicted *temperature-versus-misfit strain* phase diagram of the investigated material. Nine phases exist in this diagram, leading to four multiphase points (denoted by K , L , M , and N) where four phases “meet” each other. Note that some piezoelectric and dielectric coefficients should be rather large around these multiphase points, which could thus lead to the

development of novel efficient devices. Among the nine phases depicted in Fig. 1, four exist in PZT films under short-circuit boundary conditions [10]. They are (1) the p (paraelectric) phase [4], that has no AFD condensation and happens for high enough temperature at any investigated strain; (2) the $p[R(c)]$ state that is paraelectric too, but also exhibits long-range antiphase oxygen octahedra tilting about the *out-of-plane* direction that occurs for large compressive strain at low temperatures; (3) the aa phase [4] for large tensile strains and intermediate temperatures, for which the polarization is aligned along the in-plane $[110]$ direction and that has no long-range-ordered oxygen octahedral tilting; and (4) the $aa[R(aa)]$ state that appears for large tensile strain and low temperature, and for which the direction of the polarization and the axis about which the long-range antiphase oxygen octahedra tilt are both along the same in-plane $[110]$ direction. Out of the other five phases, only one does not exhibit FE domains. This is the state denoted as $aa[R(aac)]$ that happens for small tensile strain and low temperature and is characterized by an in-plane polarization lying along $[110]$, and by oxygen octahedral tilting in antiphase manner about a “monoclinic” $\langle uuv \rangle$ direction. Finally, the four domain states are as follows: (i) the c^d state that exhibits 180-degree nanostripe domains (alternating along an in-plane $\langle 010 \rangle$ direction) for the z -components of the dipoles, and which is the state that has been observed in $PbTiO_3$ films [8]; (ii) the aac^d phase that possesses an in-plane polarization along $[110]$ in addition to these out-of-plane nanostripes. It is similar to the “Phase II” state recently discovered in some $BaTiO_3/SrTiO_3$ superlattices [23]; (iii) the $c^d[R(c)]$ phase that exhibits long-range oxygen octahedral tilting in an antiphase fashion about the $[001]$ direction, coexisting with domains for the z -components of the dipoles; and (iv) the $aac^d[R(aac)]$ state that differs from the aac^d phase by the existence of long-range AFD tilting about a $\langle uuv \rangle$ direction. Note that these four domain states occur because OC boundary conditions prevent the existence of an overall z -component of the polarization (to remove the depolarizing field), while compressive strain favors the formation of the z -component of the electric dipoles [9].

To the best of our knowledge, the $c^d[R(c)]$ and $aac^d[R(aac)]$ states have never been previously reported. Figures 2 (a) and (b) provide a microscopic view of the dipolar and AFD configurations, respectively, in the $c^d[R(c)]$ phase. In order to understand the role of the *coupling* between electric dipoles and antiferrodistortive motions on such configurations, two other patterns are displayed in Figs. 2 (c) and (d). They correspond to the organization of electric dipoles and AFD motions, respectively, *when their mutual coupling is neglected*. Interestingly, Figs. 2(a) and 2(c) indicate that the electric dipoles rotate from the out-of-plane to in-plane directions when approaching the surfaces. Such rotation occurs in order to close the flux of 180-degree domains, and

has been just recently observed in PZT films [24]. Moreover, the FE domains have a width of 6 lattice constants, which is consistent with the equilibrium width found both theoretically and experimentally in PZT and PbTiO_3 films having the studied thickness of 4.8 nm [8,25]. Such an equilibrium width explains our choice for the lateral sizes of the supercell. Figures 2 further reveal several interesting features. For instance, the coupling between *FE* and *AFD* degrees of freedom leads to the axes of the tilting of the oxygen octahedra deviating more from the out-of-plane direction (compare Figs. 2d and 2b). The electric dipoles also adopt a more pronounced vortex-like pattern across the domain walls when the coupling between *FE* and *AFD* degrees of freedom is allowed (compare Figs. 2c and 2a), with the two vortices – one at the junction between ‘up’-‘down’ and the other one at the junction between ‘down’-‘up’ domains – having opposite chiralities. Another remarkable feature revealed by Figs. 2 is that the *AFD* degrees of freedom are strongly inhomogeneous since large *AFD* vectors coexist with small oxygen octahedral tilting. We numerically found that such inhomogeneities have two origins when the *FE*-*AFD* coupling is allowed: (i) oxygen octahedral tilting is much stronger around *Zr* atoms than around *Ti* atoms (which also explains why long-range *AFD* motions condense at higher temperature in PZT solid solutions with larger *Zr* compositions [14]); (ii) large values of the electric dipoles (such as those in the center of domains) typically lead to small *AFD* distortions because of the *competing* nature [26] of the coupling between *FE* and *AFD* degrees of freedom. Conversely, domain walls possess smaller electric dipoles -- because of the energetic cost associated with dipoles having different directions -- and therefore typically exhibit large *AFD* motions. Interestingly, items (i) and (ii) explain why we numerically found that some domain walls are *chemically pinned*, i.e. that they occur in regions possessing a concentration of *Zr* atoms larger than the average composition. However, *not all* the domain walls have to occur in *Zr*-rich regions since the domain period is also governed by the film thickness via the Kittel law [25,27,28]. All these facts are emphasized in Fig. 2(e) that displays the average magnitudes of the electric dipoles and *AFD* motions in the different (x,z) planes (these planes are perpendicular to the direction along which the ‘up’ and ‘down’ domains alternate). Figure 2e clearly relates the *AFD* magnitude with the amount of *Zr* atoms in these planes, and reiterates that electric dipoles are significantly suppressed at the domain walls while the *AFD* motions increase there. (Note also that Fig. 2e clearly shows that inside the domains, the oxygen octahedral tilting is restrained while the magnitude of the dipoles is at its maximum value). For instance, in Planes 9-10 (that coincide with the right domain wall of Fig. 2a), the *Zr* composition is the largest among all the (x,z) planes (around 55%) and the *AFD* motions are maximal, while the averaged electric dipole is

rather small. In Planes 3-4 (left domain wall) the *Zr* concentration is just slightly smaller, namely around 54%. This creates ideal conditions (i.e., small dipoles because of large *AFD* motions) for the formation of the second dipolar domain wall (again, the domain width is 6 primitive lattice constants for the chosen film thickness). Such opposite conduct of electric dipoles and *AFD* motions is consistent with the phenomenological work of Ref. [29], and can be considered as a “universal response” of the wall structure to a *competing* (biquadratic) coupling between *FE* and another degree of freedom. Moreover, the local variation in *Zr* content brings a considerable interference in this overall picture by influencing the magnitude expression of competing degrees of freedom and, therefore, the location of domain walls. Such latter fact is further evidenced when realizing that our simulations show that the removal of the coupling between *FE* and *AFD* motions leads to a repositioning of domain walls and even to a change of the direction along which such domains alternate (compare Fig. 2a and 2c).

Let us now focus on the $aac^d[R(aac)]$ state. Figures 3 show a snapshot of its associated dipolar and antiferrodistortive patterns. Comparing Figs. 2(a,b) and 3(a,b) reveals a significant deflection of both the local dipole moments and the axes about which the oxygen octahedra tilt away from the *out-of-plane* direction when going from the $c^d[R(c)]$ to $aac^d[R(aac)]$ phases, and, consequentially, a progressive growth in the average values of the *in-plane* components of polarization inside domains as the strain goes towards smaller-in-magnitude negative values. Moreover, with decrease in compressive strain, the vortex pattern for the dipoles has its center expelled toward the surfaces and possesses a more accentuated chirality (compare Figs. 2a and 3a). The resulting “cylindrical bubbles” (that are infinite along the *x*-axis) can be considered as the remnants of domain walls. Interestingly, the coexistence of these cylindrical chiral bubbles with an in-plane polarization leads to the formation of dipolar waves inside the films (see Fig. 3a). Eventually, as strain goes towards its tensile region, these cylindrical bubbles and dipolar waves both disappear and the system undergoes the transition from the $aac^d[R(aac)]$ phase to the monodomain $aa[R(aac)]$ state at low temperature. Note that these cylindrical bubbles differ from the nanobubbles previously reported in some ferroelectric or ferromagnetic systems in that the latter bubbles (1) are three-dimensional in shape (they are finite along *x*-, *y*- and *z*-directions) and (2) possess dipoles being antiparallel to the dipoles located outside these bubbles [30,31].

We hope that our predictions about the existence of novel phases and the discovery of striking morphological features in ferroelectric ultrathin films -- all resulting from the interplay between strain, alloying, electric dipoles and oxygen octahedral tilting -- will be experimentally

confirmed soon. It will also be interesting to determine if the presently discovered dipolar waves and expulsion of chiral bubbles towards the surface can also occur in ferromagnetic ultrathin films. Furthermore, our results can be beneficial to better understand *multiferroic* thin films too since these latter also exhibit a strain-dependent competition between electric dipoles and oxygen octahedral tilting [32]. We are therefore confident that the present work will result in a deeper knowledge of the fascinating fields of dipolar nanostructures and phase transitions.

This work is supported by ONR Grants N00014-04-1-0413, N00014-08-1-0915 and N00014-07-1-0825 (DURIP), NSF grants DMR-0701558 and DMR-0080054 (C-SPIN), and DOE grant DE-SC0002220. Some computations were made possible thanks to the MRI NSF grant.

-
- [1] J.F. Scott, Ann. Rev. Mater. Sci. **28**, 79 (1998).
 - [2] M. Dawber, K. M. Rabe and J. F. Scott, Rev. Mod. Phys. **77**, 1083 (2005).
 - [3] I. Kornev, H. Fu and L. Bellaiche, J. Mater. Sci. **4**, 137 (2006).
 - [4] N. A. Pertsev, V. G. Kukhar, H. Kohlstedt, and R. Waser, Phys. Rev. B **67**, 054107 (2003).
 - [5] O. Dieguez, S. Tinte, A. Antons, C. Bungaro, J. B. Neaton K.M. Rabe, and D. Vanderbilt, Phys. Rev. B **69**, 212101 (2004).
 - [6] B.-K. Lai, I.A. Kornev, L. Bellaiche, and G. J. Salamo, Appl. Phys. Lett. **86**, 132904 (2005).
 - [7] N. A. Pertsev, A. K. Tagantsev, and N. Setter, Phys. Rev. B **61**, R825 (2000), Phys. Rev. B **65**, 219901 (2000).
 - [8] S. K. Streiffer *et al*, Phys. Rev. Lett. **89**, 067601 (2002).
 - [9] I. Kornev, H. Fu, and L. Bellaiche, Phys. Rev. Lett. **93**, 196104 (2004).
 - [10] D. Sichuga, I. Ponomareva, L. Bellaiche, Phys. Rev. B **80**, 134116 (2009).
 - [11] B. Noheda, D. E. Cox, G. Shirane, S. E. Park, L. E. Cross, and Z. Shong, Phys. Rev. Lett. **86**, 3891 (2001).
 - [12] L. Bellaiche, A. Garcia, and D. Vanderbilt, Phys. Rev. Lett. **84**, 5427 (2000); Ferroelectrics **266**, 41 (2002).
 - [13] K. Uchino, *Piezoelectric Actuators and Ultrasonic Motors* (Kluwer Academic Publishers, Boston, 1996).
 - [14] I.A. Kornev, L. Bellaiche, P.-E. Janolin, B. Dkhil, and E. Suard, Phys. Rev. Lett. **97**, 157601 (2006).
 - [15] M. Fornari, D. J. Singh, Phys. Rev. B **63**, 092101 (2001).
 - [16] B. Noheda, L. Wu, and Y. Zhu, Phys. Rev. B **66**, 060103(R) (2002).
 - [17] D.M. Hatch, H.T. Stokes, R. Ranjan, Ragini, S.K. Mishra, D. Pandey and B.J. Kennedy, Phys. Rev. B **65**, 212101 (2002).
 - [18] D.J. Woodward, J. Knudsen and I.M. Reaney, Phys. Rev. B **72**, 104110 (2005).

- [19] R. Ranjan, Ragini, S.K. Mishra, D. Pandey and B.J. Kennedy, Phys. Rev. B **65**, 060102(R) (2002).
- [20] D. Sichuga, W. Ren, S. Prosandeev, and L. Bellaiche, Phys. Rev. Lett. **104**, 207603 (2010).
- [21] I. Ponomareva, I. Naumov, I. Kornev, H. Fu, and L. Bellaiche, Phys. Rev. B **72**, 140102(R) (2005).
- [22] W. Zhong, D. Vanderbilt, and K.M. Rabe, Phys. Rev B **52**, 6301 (1995).
- [23] S. Lisenkov and L. Bellaiche, Phys. Rev. B **76**, 020102(R) (2007).
- [24] C-L Jia et al, Science **331**, 1420 (2011)
- [25] B-K. Lai, I. Ponomareva, I. A. Kornev, L. Bellaiche and G. J. Salamo, Appl. Phys. Lett. 91, 152909 (2007).
- [26] D. Vanderbilt and Z. Zhong, Ferroelectrics **206-207**, 181 (1998).
- [27] L. Landau and E. Lifshitz, Phys. Z. Sowjetunion 8, 153 (1935).
- [28] C. Kittel, Phys. Rev. 70, 965 (1946).
- [29] B. Houchmandzadeh, J. Lajzerowicz, and E. Salje, J. Phys.: Condens. Matter **3**, 5163 (1991).
- [30] B.-K. Lai, I. Ponomareva, I. I. Naumov, I.A. Kornev, H. Fu, L. Bellaiche and G. J. Salamo, Phys. Rev. Lett. **96**, 137602 (2006).
- [31] A. Hubert and R. Schafer, *Magnetic Domains: The Analysis of Magnetic Microstructures* (Springer, Berlin, 1998).
- [32] I.C. Infante *et al*, Phys. Rev. Lett. **105**, 057601 (2010).

FIGURE CAPTIONS:

FIG.1. Temperature-versus-misfit-strain phase diagram of a $\text{Pb}(\text{Zr}_{0.52}\text{Ti}_{0.48})\text{O}_3$ ultrathin film of 4.8 nm thickness and under open-circuit electrical boundary conditions. K, L, M, and N indicate multiphase points where four phases meet, while the different structural phases displayed in this diagram are explained in the text.

FIG.2. (color online) 10 K pattern of the electric dipoles (Panel a) and AFD vectors (Panel b) in a (y,z) plane for the $c^d[\text{R}(c)]$ state of a 4.8nm-thick PZT film under a compressive strain of -2%, as mimicked by a $12 \times 12 \times 12$ supercell. Panels (c) and (d) show similar data in a (x,z) plane that Panels (a) and (b), respectively, but when the couplings between FE and AFD degrees of freedom are turned off. The vortex-type pattern of the electric dipoles near the domain walls is highlighted by means of ovals in Panel (a). The blue (respectively, red) color in Panels (a)-(d) refers to the z-component of the dipoles or AFD vectors being positive (respectively, negative). Panel (e) displays the dependency of the average magnitude of the electric dipoles (left ordinate axis) and AFD vectors (right ordinate axis) as a function of the (x,z) plane index, when the coupling between FE and AFD motions is allowed. The position of the ferroelectric domain walls are indicated by arrows in Panels (a), (b), and (c), and by vertical dotted lines in Panel (e). Numerical values above the Panel (e) illustrate the number of Zr atoms out of the 144 atoms belonging to each (x,z) plane.

FIG.3. (color online) 10 K pattern of the electric dipoles (Panel a) and AFD vectors (Panel b) in a (y,z) plane for the $aac^d[\text{R}(aac)]$ state of the 4.8nm-thick PZT film under a compressive strain of -0.25%, as mimicked by a $12 \times 12 \times 12$ supercell. The “cylindrical chiral bubbles” formed by the electric dipoles are highlighted by means of ovals in Panel (a). The dipolar waves are also highlighted by means of a solid line in that Panel. The blue (respectively, red) color refers to the z-component of the dipoles or AFD vectors being positive (respectively, negative).

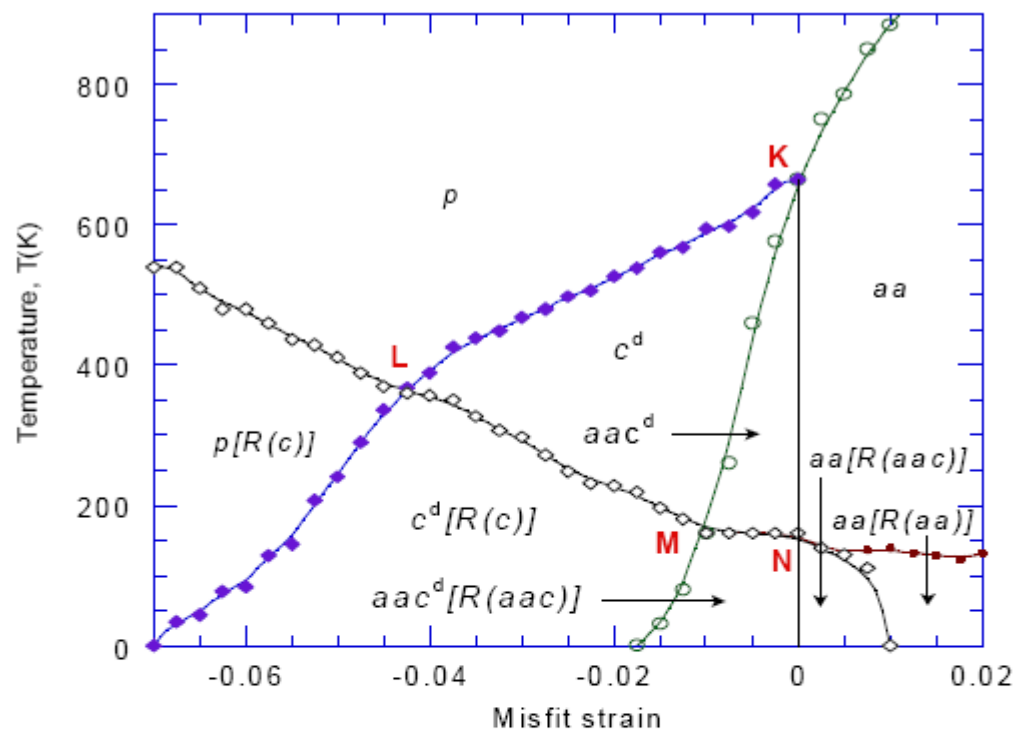


Figure 1

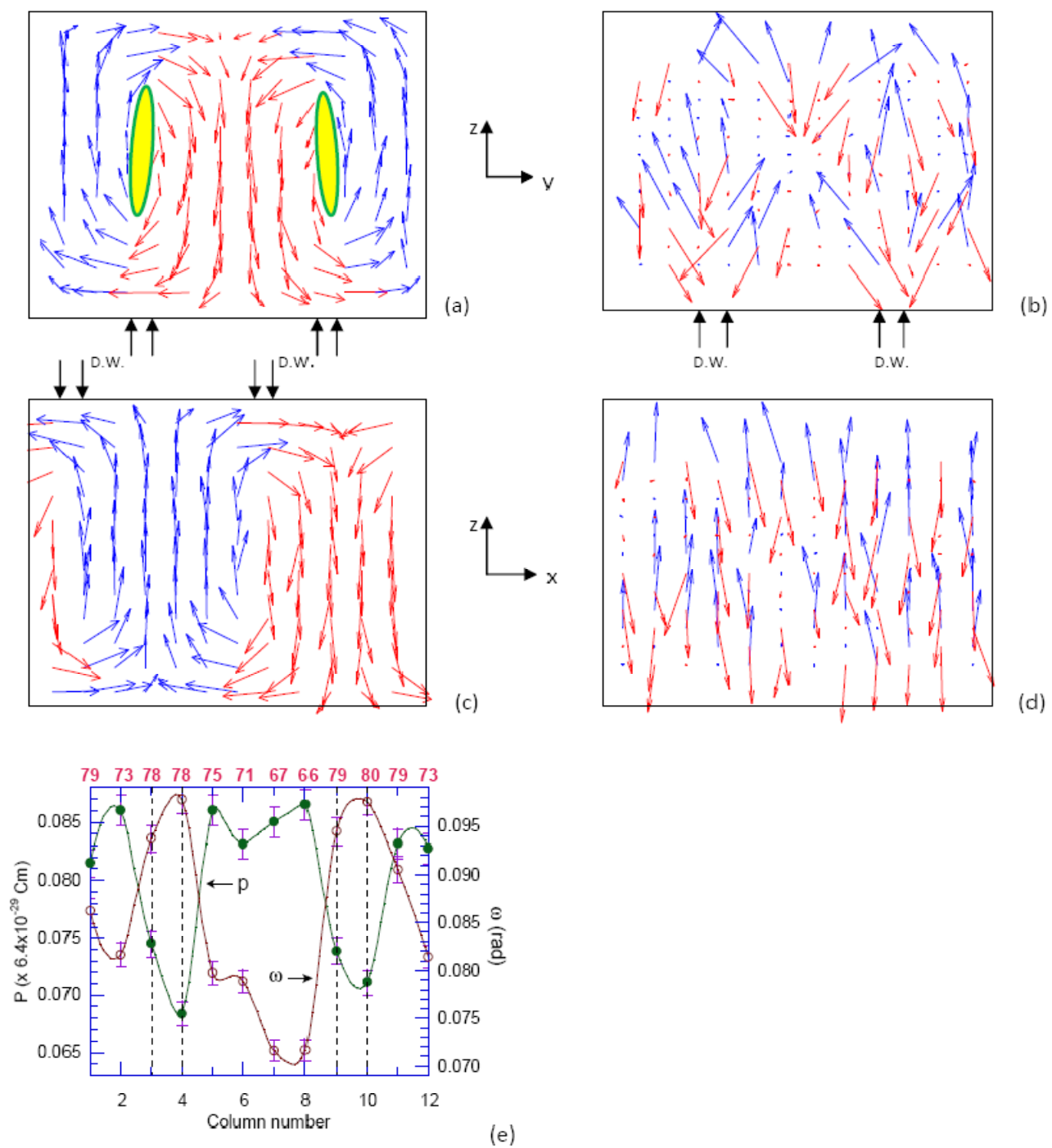


Figure 2

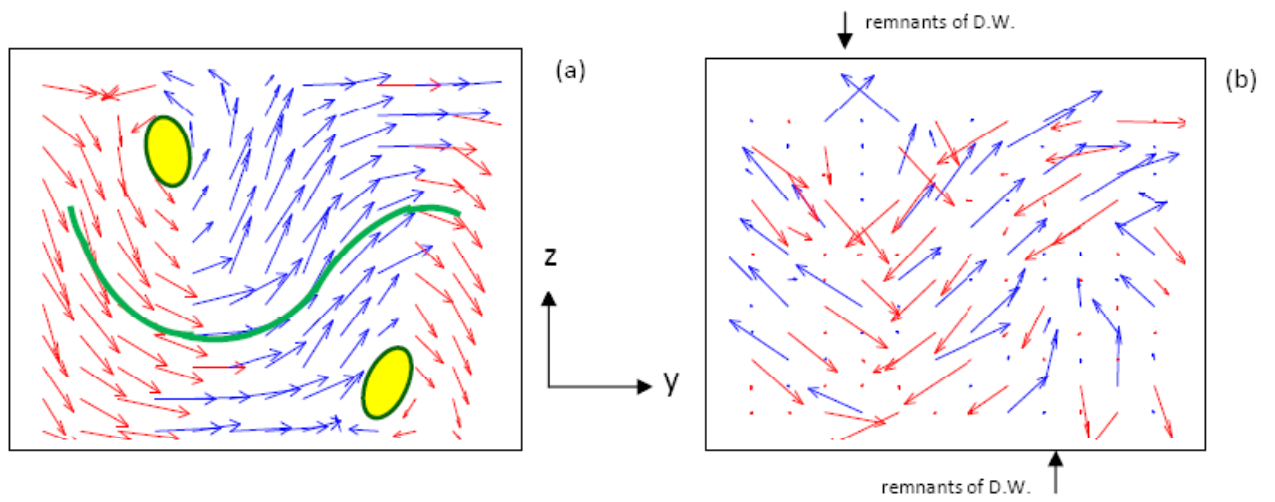


Figure 3